Accurate Underwater Optical Wireless Communication Model With Both Line-of-Sight and Non-Line-of-Sight Channels

Chengwei Fang, *Graduate Student Member, IEEE*, Shuo Li, *Member, IEEE*, and Ke Wang, *Member, IEEE*

***Abstract*—Underwater optical wireless communication (UOWC) systems have been widely studied to achieve high-speed wireless communications. To investigate and design UOWC systems, a mathematical model to characterize the accurate performance of UOWC systems is important. However, the previous mathematical models of UOWC systems have limitations, which mainly focused on the line-of-sight (LOS) link, and only considered the vertical incident background light or optical filters with constant transmittance for simplicity. To overcome these limitations, we establish an accurate UOWC system model, incorporating the previously overlooked impact of signal and sun lights incident angles and including both LOS and non-line-of-sight (NLOS) channels. Our proposed accurate UOWC system model is validated by Monte Carlo (MC) simulations. Results show that our proposed model can capture the changes of received powers of both signal and background lights with various transmitter and receiver alignments and orientations in both LOS and NLOS channels, which typically affect the signal-noise-ratio (SNR) and bit-error-rate (BER) performance of UOWC systems. Furthermore, we show that the incident angles of both signal and sun lights have significant impact on the system performance, and our proposed model can be used to optimize the PD rotation angle to improve the SNR performance. Therefore, the more accurate UOWC channel model established in this paper provides a fundamental framework for future UOWC system design and optimization.**

***Index Terms*—Underwater optical wireless communication, line-of-sight, none-line-of-sight, variable incident angles.**

I. Introduction

In THE past a few years, the underwater wireless communication (UWC) has attracted intensive attention due to the large range of applications such as underwater wireless sensor networks, autonomous underwater vehicles (AUV), ocean exploration, and underwater defence systems. With the real-time communication need, higher transmission speed is demanded than ever in UWC systems. The traditional UWC mainly relies on the underwater acoustic communication (UAC), which has been explored to transmit data for long-distance reaching up to several tens of kilometres [1]. However, UAC suffers from a low data rate due to the low modulation bandwidth (only kHz) [2]. The propagation speed of acoustic waves in the underwater channel is also slow, leading to a latency of about 0.67 s per kilometre [3]. Compared to UAC, underwater radio frequency (RF) communication suffers from a high attenuation in underwater channels, which leads to a highly limited transmission distance [4]. Thus, RF communication is not adopted.

To overcome the disadvantage of the UAC with high latency and low data rate, UOWC has been proposed and widely studied due to its great potential to achieve a high data rate reaching Gbps, thanks to the high carrier frequency and modulation bandwidth (exceeding MHz [5] and even GHz [6]). Moreover, the physical transmission latency is about 4.34 μs per kilometre, which is much lower than the latency of acoustic waves in the underwater channel. These high-speed and low-latency advantages will enable many real-time applications, such as real-time underwater detection systems, and real-time communication between AUV and diver. Furthermore, UOWC is more cost-effective and power-efficient compared to those of UAC, benefiting from low-cost and low-power transceivers such as light-emitting diodes (LEDs), laser diodes (LDs), and photodiodes (PDs) [7]. However, the transmission distance of UOWC is highly limited (only hundreds of meters in tap water channel [8]), mainly due to the high attenuation of water (particularly seawater) and the background light noise that reduce the signal-to-noise ratio (SNR).

To investigate the capability and limitation of UOWC systems, an accurate UOWC channel model needs to be established first. In [9], the authors established a basic theoretical LOS UOWC mathematical model. Whilst the incident angle of signal light was considered, only vertical incident background light was included. In addition, the optical filter was ignored in the study. In [10], the authors presented a LOS model of a UOWC channel using the vector radioactive transfer theory. They considered the optical filter in the solar noise model. However, the transmittance of the optical filter was considered as a constant for simplicity. Furthermore, in [11], the authors presented a LOS UOWC system model. They investigated the impact of solar background light on the UOWC system performance and presented the simulation results for receivers with variable field-of-view (FOV) and aperture diameters. However, only vertical incident background light was considered. In fact, as the position of the earth and the sun changes over time, the angle at which the sun light enters

Manuscript received 9 August 2022; revised 10 October 2022; accepted 18 October 2022. Date of publication 25 October 2022; date of current version 7 November 2022. This work was supported by the Australian Research Council (ARC) under Grant DP170100268. *(Corresponding author: Chengwei Fang.)*

The authors are with the School of Engineering, Royal Melbourne Institute of Technology (RMIT) University, Melbourne, VIC 3000, Australia (e-mail: chengweifang907@gmail.com; shuo.li2@rmit.edu.au; ke.wang@rmit.edu.au).

Digital Object Identifier 10.1109/JPHOT.2022.3216599

the water surface cannot be considered as vertical all the time. Similar to previous studies, the transmittance of the optical filter was assumed to be constant for simplicity as well.

In addition to the limitations discussed above, the previous studies [9], [10], [11] have also ignored the dependence of filter transmittance on the light wavelength. Nevertheless, a few studies have considered such dependence. For instance, in a recent study [12], the UOWC system performance was studied incorporating the effect of multipath and the impact of wavelength. Simulation results with variable incident angles of both signal and background lights are provided. However, the transmittance of the band-pass filter only changes with signal and background lights wavelength, which is not accurate ignoring the incident angle of lights. From the discussions above, it is clear that due to the use of constant transmittance of optical filters, the impact of the incident angle of both signal and background lights has been largely neglected in previous works. Moreover, in most previous work, researchers have focused on the LOS UOWC system models. On the other hand, NLOS UOWC systems are important in underwater channels when the LOS links are blocked by marine biology or complex underwater topography, whilst only a few studies have investigated NLOS UOWC models. In [13] and [14], the authors investigated both LOS and NLOS UOWC system performance with the impact of solar noise. However, only vertical-incident sun light was considered, and similar with other prior works, a constant transmittance of the filter was applied for simplify.

To overcome these limitations, in this paper we establish an accurate UOWC channel model incorporating the impact of incident angles of both signal and sun lights and considering both LOS and NLOS links. We verify our mathematical model by MC simulations considering scattering [15]. Results show that the discrepancy is minimal and our proposed theoretical results agree well with MC simulations, which verifies the accuracy of both LOS and NLOS UOWC model in different sea channels. We also use this model to study the UOWC system performance in terms of the signal-to-noise ratio (SNR) and bit-error-rate (BER). Results show that the incident angles of both signal and sun lights have significant impact on the system performance. In addition, previous models cannot capture the signal and solar optical powers at the receiver side accurately, due to the simplified assumption of constant transmittance of optical filters. On the other hand, our proposed model can capture the fluctuation of received optical power with the variable incident angles of both signal and sun lights. Moreover, based on the model developed, we further investigate the signal transmission performance by optimizing the PD orientation.

The remainder of the paper is organized as follows. In Section II-A we present our proposed LOS UOWC channel model considering variable incident angles of signal and sun lights, and we verify the model with MC simulations in Section II-B. Then we apply the proposed model in practical LOS UOWC systems to study the SNR and BER performances in Section II-C. In Section III, we further present our proposed NLOS UOWC channel model, verify it by MC simulations, and study the SNR and BER performances of NLOS UOWC systems using the model. Finally, we conclude our work in Section IV.

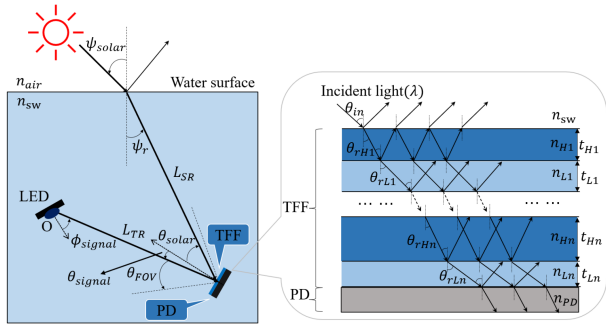

Fig. 1. LOS UOWC system architecture.

II. LOS UOWC System and Simulation

A. LOS Theoretical Model

In this section, we present our proposed accurate LOS UOWC system model, which considers a typical LOS communication link shown in Fig. 1. It consists of the optical transmitter, the optical receiver, the underwater channel, and the solar light. We consider the LED-based transmitter and pure seawater channel [16]. For the receiver, it contains an optical filter and an optical detector, which is a thin-film-based optical filter (TFF) and a PIN photodiode (PD), respectively. Note that the channel model can also be applied to laser-based transmitters and other types of seawater channels, optical filters, and detectors. At the receiver side, in addition to the LOS signal passing through the pure seawater channel, the sun light after being refracted by the air-water interface and passing through the seawater is also detected, which introduces solar noise. Before the signal and solar lights being converted to the electrical domain by the PIN PD, they pass through the TFF, which uses the principles of light interference and diffraction to reduce the influence of out of band background light. When the light with different wavelengths reaches the receiver, only the light within a specific wavelength band (signal light) has constructive interference to pass through the TFF and be detected by the PD. On the other hand, the out of band light is filtered out to avoid saturation or additional background light noise. We call the optical power change of light in the specified wavelength range after passing through the optical filter as the transmittance. As discussed below, the light incident angle (θ_{in}) affects the transmittance, and hence, affects the actual optical signal and solar lights that are converted by the PD. However, this important factor has been ignored in previous works. It is noted that our aim here is not to investigate the physical aspect of an optical filter, but rather to focus on the impact on the channel model and the subsequent link performance when the signal and sun lights incident angles vary in practical scenarios.

There are two types of transmitters in UOWC systems, which are the LED and the laser. The LED-based transmitter has the advantages of the low cost and low power consumption. However, due to the wide beam divergence, the power decreases sharply with the orientation angle ϕ_{signal} of LED. Hence, LED-based transmitters are widely used in short-distance UOWC systems. On the contrary, the laser-based transmitter has the advantage

of a collimated beam, which is more suitable for long-distance UOWC. Here we consider an LED-based transmitter, which is modeled as a Lambertian source. The considered channel model can also be applied to laser-based transmitters, where a Gaussian profile can be used to model the emitted laser light. When the light propagates through the seawater channel, general turbidity in seawater leads to the absorption and scattering, which causes light losing power. It can be characterized by the signal path loss $L_{signal,p}(\lambda)$, which is dependent on the seawater attenuation coefficient $c(\lambda)$ and the seawater channel length. The attenuation of seawater can be expressed by [17]

$$c(\lambda) = a(\lambda) + b(\lambda). \tag{1}$$

where $a(\lambda)$ is the absorption coefficient, and $b(\lambda)$ represents the scattering coefficient.

Hence, the signal path loss can be expressed as [13]

$$L_{signal,p}(\lambda) = e^{-c(\lambda)L_{TR}} = e^{-[a(\lambda)+b(\lambda)]L_{TR}}, \tag{2}$$

where L_{TR} denotes the Euclidean distance between the LED transmitter and the receiver.

After passing through the seawater channel, the signal is collected by the receiver. Due to the beam divergence of LED and the limited aperture of the receiver, only part of the signal light can be collected. We introduce the loss due to the smaller receiver aperture size compared with the signal beam footprint as the geometrical loss, which is expressed as [18]

$$L_{signal,g} = \frac{m+1}{2\pi}\cos^m(\phi_{signal})\Delta\Omega, \tag{3}$$

where ϕ_{signal} denotes the optical irradiance angle of the LED, as shown in Fig. 1. $m = -\frac{\ln 2}{\ln(\cos\phi_{1/2})}$ is the Lambertian order, where $\phi_{1/2}$ is the semi-angle at half emitted optical power, and $\Delta\Omega$ is the solid angle subtended by the receiver differential area. If we assume $A_f << L_{TR}^2$, it can be given by $\Delta\Omega = \frac{A_f\cos\theta_{signal}}{L_{TR}^2}$, where $A_f = \pi r_{PD}^2$ is the input area of the PD, and it is assumed to match the size of the TFF with r_{PD} representing the radius of PD. θ_{signal} is the incident angle of the signal light to the receiver, also shown in Fig. 1.

Before being converted by the PD, the signal light propagates through the optical filter in front of the PD, which is used to reject the out-of-band background light to reduce the receiver noise. In this paper, we consider the TFF, which is the most widely used filter in UOWC systems [19]. The structure of TFF is shown in Fig. 1, which consists of multiple layers of alternating high and low refractive index films. The thickness and refractive index of each layer are selected according to the filter pass-band requirements. Due to the low transmission loss of the blue light, we consider a blue light transmitter in UOWC systems. Hence, we use a blue-pass filter here to enhance the system performance. When the light enters the filter, lights of different wavelengths are refracted and reflected at different angles. After multiple refractions and reflections, only lights with specific wavelengths can pass through the filter and be collected by the PD. We denote the transmittance of TFF as $T_f(\lambda,\theta_{in})$, which is the ratio of transmitted optical power after optical filter to the incident optical power, and it can be described as (4), shown at the bottom of the page [20], where $\gamma_0 = n_{sw}\sqrt{\epsilon_0\mu_0}$ and $\gamma_S = n_{PD}\sqrt{\epsilon_0\mu_0}$ are transmittance parameters, n_{sw} denote the refractive index of the seawater [21], n_{PD} denotes the refractive index of the photo-detector input aperture [20], ϵ_0 is the permittivity of free space, and μ_0 denotes the permeability of free space.

M_λ represents the transmission matrix of the filter, which can be calculated as (5) shown at the bottom of the page [20], where N denotes the number of layers used in filter. In the transmission matrix, $\gamma_H = n_H\sqrt{\epsilon_0\mu_0}$, $\gamma_L = n_L\sqrt{\epsilon_0\mu_0}$, $\delta_H(\lambda) = \frac{2\pi}{\lambda}n_H l_H$, and $\delta_L(\lambda) = \frac{2\pi}{\lambda}n_L l_L$, where n_H and n_L are the refractive indices of alternating high index and low index layers, and $l_H = \frac{t_H}{\cos(\theta_{rH})}$ and $l_L = \frac{t_L}{\cos(\theta_{rL})}$ denote the light path lengths in the high index layer and the low index layer, respectively, where t_H and t_L stand for the thickness of these layers, and θ_{rH} and θ_{rL} denote the light refraction angles in these layers, related with the light incident angle θ_{in} shown in Fig. 1 following the Snell's law.

After passing through the TFF, the power of the optical signal reaching the PD can be expressed as (6), shown at the bottom of the page, where the $P_t(\lambda)$ is the emitted optical power of the LED, $\lambda_{signal,h}$ and $\lambda_{signal,l}$ denote the range of signal light that can be detected in the system. There are two possibilities: within FOV or outside FOV. When outside FOV, no power is received, and within FOV, we add together the power of different wavelengths, and for each wavelength, the power is $P_t(\lambda)d\lambda$.

Then, we consider the water surface solar spectral downwelling plane irradiance $E_{sun}(\lambda)$ in $\mathrm{W}\cdot\mathrm{m}^{-2}\cdot\mathrm{nm}^{-1}$ [11], shown in Fig. 1, where λ is the wavelength of the light in vacuum. Since the sun light can be considered as parallel, only part of the sun light incident onto the water surface can reach

$$T_f(\lambda,\theta_{in}) = 100\left(\left|\frac{2\cdot\gamma_0}{\gamma_0\cdot(M_\lambda)_{1,1}+\gamma_0\cdot\gamma_S\cdot(M_\lambda)_{1,2}+(M_\lambda)_{2,1}+\gamma_S\cdot(M_\lambda)_{2,2}}\right|\right)^2 \tag{4}$$

$$M_\lambda = \left\{\begin{bmatrix}\cos(\delta_H(\lambda)) & \frac{i\cdot\sin(\delta_H(\lambda))}{\gamma_H}\\ i\cdot\gamma_H\cdot\sin(\delta_H(\lambda)) & \cos(\delta_H(\lambda))\end{bmatrix}\cdot\begin{bmatrix}\cos(\delta_L(\lambda)) & \frac{i\cdot\sin(\delta_L(\lambda))}{\gamma_L}\\ i\cdot\gamma_L\cdot\sin(\delta_L(\lambda)) & \cos(\delta_L(\lambda))\end{bmatrix}\right\}^N \tag{5}$$

$$P_{signal,r,LOS} = \begin{cases}\int_{\lambda_{signal,l}}^{\lambda_{signal,h}} P_t(\lambda)L_{signal,p}(\lambda)L_{signal,g}T_f(\lambda,\theta_{signal})d\lambda, & 0\le\theta_{signal}\le\theta_{FOV}\\ 0. & \theta_{signal}>\theta_{FOV}\end{cases} \tag{6}$$

the receiver. We introduce the effective area of solar radiation at the water surface that can reach the receiver as A_{solar}, which can be expressed as

$$A_{solar} = A_f \frac{\cos\theta_{solar}}{\cos\psi_r}, \tag{7}$$

where θ_{solar} denotes the sun light incident angle to the receiver, and ψ_r is the sun light refraction angle into the water. According to Snell's law, $\psi_r = \arcsin(\frac{n_{air}}{n_{sw}}\sin\psi_{solar})$, where n_{air} represent the refractive index of the air, and ψ_{solar} is the sun light radiation angle to the water. In previous studies, the sun light radiation angle has been mostly considered as 0° (i.e., vertical) for simplicity. However, as shown later, such simplified assumption leads to the sun light power at the receiver being significantly overestimated.

When the sun light reaches the ocean-air surface, some is reflected and some is refracted. This causes the propagation refraction loss, which can be expressed as [13]

$$L_{solar,r} = 1 - \frac{1}{2}\left[\left(\frac{\tan(\psi_r - \psi_{solar})}{\tan(\psi_r + \psi_{solar})}\right)^2 + \left(\frac{\sin(\psi_r - \psi_{solar})}{\sin(\psi_r + \psi_{solar})}\right)^2\right], \tag{8}$$

With both scattering and absorption considered, the solar path loss is approximated as

$$L_{solar,p}(\lambda) = e^{-c(\lambda)L_{SR}} = e^{-[a(\lambda)+b(\lambda)]L_{SR}}, \tag{9}$$

where L_{SR} stands for the Euclidean distance between the central point of the solar radiation effective area and the optical receiver.

It is clear from (4) and (5) that the transmittance of the optical filter at the receiver side of UOWC systems is highly dependent on the light incident angle. Hence, the solar power detected by the PD can be expressed as (10) shown at the bottom of this page, where $\lambda_{solar,h}$ and $\lambda_{solar,l}$ denote the range of sun light that can be detected in the system. Similar to signal case, when outside FOV, no solar background light power is received, and within FOV, we add together the power of different wavelengths, and for each wavelength, the power is $E_{sun}(\lambda)A_{solar}d\lambda$.

With the signal and sun lights modeled in (6) and (10), here we further consider the SNR of LOS-based UOWC system to better characterize the wireless communication performance. The SNR can be calculated as

$$SNR_{LOS} = \frac{\mu^2_{signal,LOS}}{\sigma^2_{total}} = \frac{(\Re P_{signal,r,LOS})^2}{\sigma^2_{total}}. \tag{11}$$

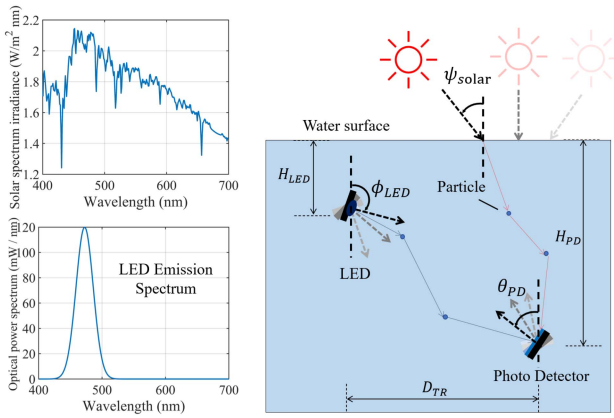

Fig. 2. LOS UOWC system setting in the Monte Carlo simulation.

where $\mu^2_{signal,LOS}$ denotes the signal electrical power, and $\Re$ denotes the PD responsivity. In UOWC systems with PIN PD [9], [10], the major noises consist of the solar background noise σ^2_{so}, blackbody noise σ^2_{bl}, dark current noise σ^2_{DC}, signal shot noise σ^2_{ss}, and thermal noise σ^2_{TH}, which can be expressed as (12), shown at the bottom of this page, where $q = 1.6 \times 10^{-19}$ denotes the elementary charge, B is the bandwidth, $P_{blackbody}$ represents the blackbody radiation power [10], I_{DC} denotes the PD dark current, k is the Boltzmann's constant, T_e is the equivalent temperature, F represents the noise figure, and R_L is the load resistance.

Based on SNR, the BER of the LOS-based UOWC link can be further calculated. Here we consider the on-off-keying (OOK) symbol modulation that is widely used in UOWC systems [22], and the BER can be expressed as [23]:

$$BER_{LOS,OOK} = \frac{1}{2}erfc\left(\frac{SNR_{LOS}}{2\sqrt{2}}\right). \tag{13}$$

B. Monte-Carlo Verification of LOS Channel Model

In this section, we conduct Monte-Carlo simulations to verify the LOS UOWC system model. The UOWC system considered is shown in Fig. 2, and the parameters are shown in Table I. For the signal part, n photons were generated by the LED transmitter, whose wavelength distribution followed the radiation spectrum of a typical blue LED [24], illustrated in the inset of Fig. 2. The angular distribution of photons followed the Lambertian pattern with each photon carrying a power of $P_{photon} = \frac{P_t}{n}$. The signal photons transmitted through the pure sea channel. We denote the distance before interacting with a particle in the medium as the

$$P_{solar,r} = \begin{cases} \int_{\lambda_{solar,l}}^{\lambda_{solar,h}} E_{sun}(\lambda)A_{solar}L_{solar,r}L_{solar,p}(\lambda)T_f(\lambda,\theta_{solar})d\lambda, & 0 \le \theta_{solar} \le \theta_{FOV} \\ 0, & \theta_{solar} > \theta_{FOV} \end{cases} \tag{10}$$

$$\begin{aligned}\sigma^2_{total} &= \sigma^2_{so} + \sigma^2_{bl} + \sigma^2_{DC} + \sigma^2_{ss} + \sigma^2_{TH} \\ &= 2q\Re P_{solar.r}B + 2q\Re P_{blackbody}B + 2qI_{DC}B + 2q\Re P_{signal,r,LOS}B + \frac{4kT_eFB}{R_L}\end{aligned} \tag{12}$$

TABLE I
TRANSMITTER, MEDIUM, AND RECEIVER PARAMETERS

Tx	Value	Medium	Value	Rx	Value
λ_c	472.5 nm	a (λ)	0.053	θ_{FOV}	90°
$\lambda_{LED,l}$	400 nm	b (λ)	0.003	n_{PD}	1.52
$\lambda_{LED,h}$	700 nm	c (λ)	0.056	R_L	100 Ω
$\phi_{1/2}$	30°	n_{sw}	1.33		
P_t	4080 mW				

single travel distance L_{single}, which can be expressed as [25]

$$L_{single} = -\frac{\log(N[0,1])}{c(\lambda)}, \tag{14}$$

where $N[0,1]$ denotes a random number between 0 and 1, following random distribution.

When interacting with the particle, the photon lost a fraction of power and propagated in a new direction. We denote the photon power before and after the interaction as $P_{p,be}$ and $P_{p,af}$, respectively, which can be expressed as [16]

$$P_{p,af} = P_{p,be}\left(1 - \frac{a(\lambda)}{c(\lambda)}\right), \tag{15}$$

The new propagation direction is determined by the new azimuthal angle $\phi_{signal.A}$ and scattering angle $\phi_{signal.S}$, which follow a random distribution $N[0, 2\pi]$ and the Henyey-Greenstein (HG) model or Two Term Henyey-Greenstein (TTHG) model, respectively [16]. If the signal photon reached the receiver, we recorded the incident angle to the TFF and further calculated the transmittance. Finally, we recorded the power of each photon after passing through the TFF.

Here, we considered a nine-layers blue pass TFF1 and a twelve-layers blue pass TFF2 with TiO_2 and SiO_2 layers following the parameters in [26]. Using (4) the transmittance is shown in Fig. 3(a) and (b). It is clear that $T_f(\lambda, \theta_{in})$ is highly related with the light incident angle. When the incident angle increases, the transmission peak experiences a red shift. More importantly, it is clear that simplifying the TFF transmittance as a constant in previous theoretical studies results in significant modeling errors, and the impact of light incident angle on the UOWC system needs to be incorporated.

In the system setting, the LED and the PD orientation angles ϕ_{LED} and θ_{PD} are defined as 0^o when facing up vertically. The sun light radiation angle ψ_{solar} is defined as 0° when propagating vertically downward. These angles are defined as positive when rotating in the clockwise direction. It is noted that we assumed a 90° semi-angle FOV of the receiver to better study the impact of light incident angels on UOWC systems.

In the simulation, we set the LED semi-power angle $\phi_{1/2} = 30°$ [27], which was also widely used in previous research [28], [29]. Then, we selected the absorption coefficient $a(\lambda) = 0.053$ m^{-1}, scattering coefficient $b(\lambda) = 0.003$ m^{-1}, and attenuation coefficient $c(\lambda) = 0.056$ m^{-1}, which are experimentally characterized values in previous research [16]. Here, we set the LED and PD depths at $H_{LED} = 10$ m and $H_{PD} = 15$ m, and the horizontal distance between LED and PD D_{TR} at 5 m. Moreover, we set $r_{PD} = 1$ inch and the number of photons $n = 2 \times 10^8$. Then

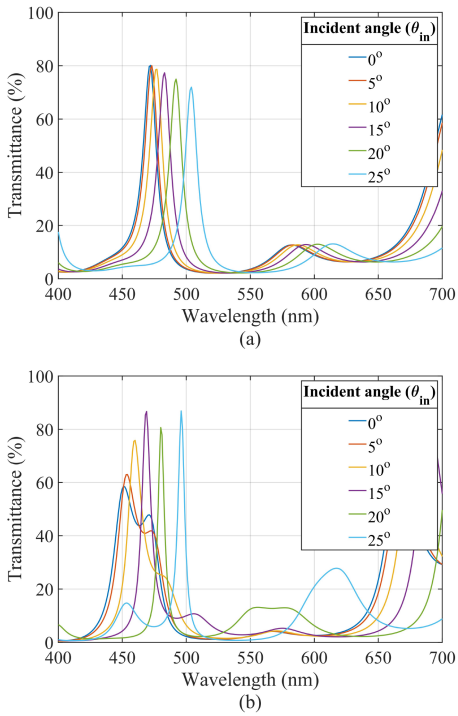

Fig. 3. (a) and (b): Transmittance v.s. light incident angle of the considered TFF1 and TFF2, respectively.

we fixed θ_{PD} at $-45°$, $-25°$ or $-5°$, and calculated the theoretical received optical powers using (6) when changing the LED orientation angle ϕ_{LED}, which were compared with MC simulations adopting two scattering models. The results are shown in Fig. 4(a).

It is clear that due to considering scattering in MC simulations, the received signal power in MC simulations is slightly higher than that obtained using the theoretical model. However, the discrepancy is minimal and the theoretical results agree well with MC simulations, which verifies the accuracy of our LOS UOWC model in the pure sea channel. Furthermore, it can be seen that the strength of signal increases when the LED is rotated towards the PD ($\phi_{LED} = 135°$ when LED directly faces PD), which is mainly due to the Lambertian pattern of the LED radiation. Moreover, the received optical power decreases when PD rotated from $-45°$ to $-5°$ for the same ϕ_{LED}. This is mainly due to the larger signal incident angle to the receiver, which leads to a red-shift and lower efficiency of the filter transmission spectrum, as shown in Fig. 3.

In addition to the received optical power, the channel impulse response (CIR) is also important, which can quantify the time dispersion [16]. Hence, we also study the CIR, and the results are shown in Fig. 4(b). It is clear that similar with the received signal power, when the LED is rotated away from the PD, less photons can reach the PD due to the Lambertian pattern of the transmitter. More importantly, the optical power drops sharply with respect to time, which indicates the small number of photons arriving at the receiver after scattering due to considering pure sea water. Hence, the impact of scattering is minimal and it further confirms the results shown in

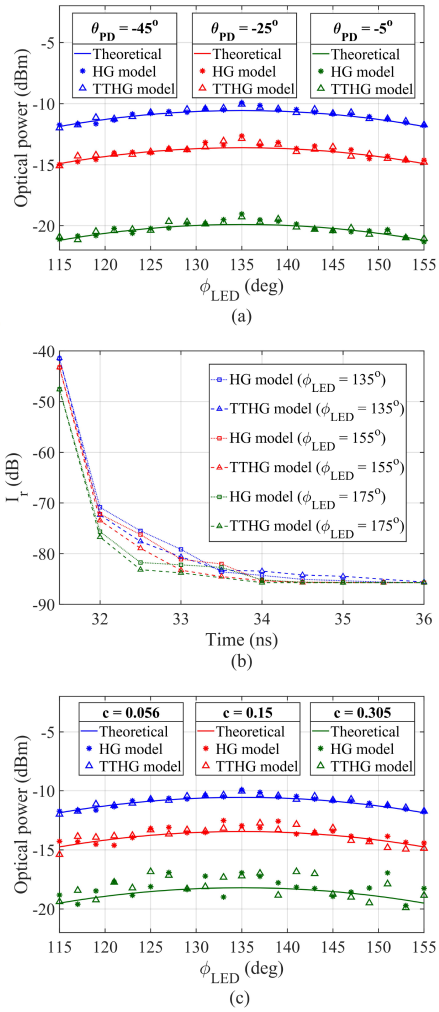

Fig. 4. LOS theoretical and MC simulation results. (a): received signal optical power v.s. LED orientation angle ϕ_{LED}; (b): CIR (received intensity as a function of time) under the PD orientation angle $\theta_{PD} = -45°$; (c): received signal optical power v.s. LED orientation angle ϕ_{LED} under different attenuation coefficient c ($\theta_{PD} = -45°$).

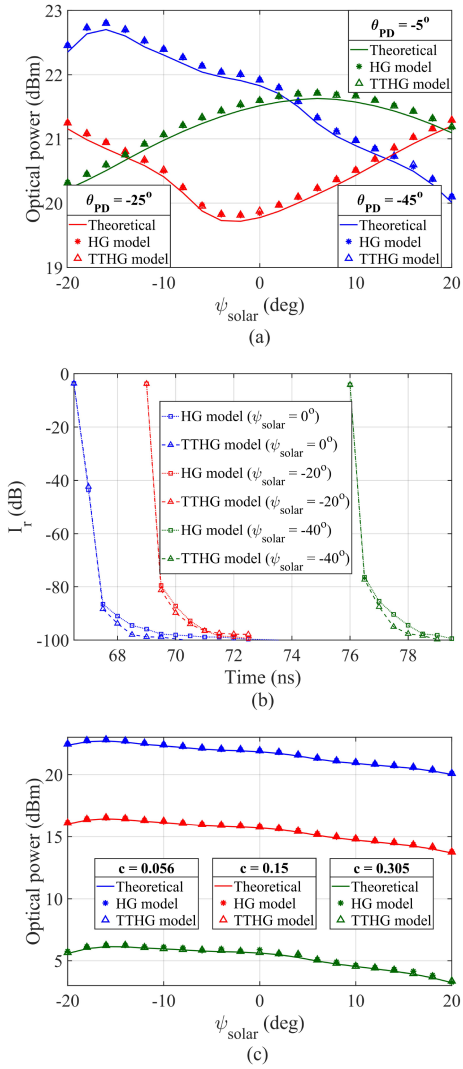

Fig. 5. Solar part theoretical and MC simulation results. (a): received solar power v.s. sun light radiation angle ψ_{solar}; (b): CIR under the PD orientation angle $\theta_{PD} = -45°$; (c): received solar power v.s. sun light radiation angle ψ_{solar} under different attenuation coefficient c ($\theta_{PD} = -45°$).

Fig. 4(a), where our theoretical results agree well with MC simulations.

Moreover, we also investigate the received signal power in sea water with different turbidity. According to [30], [31], the light attenuation coefficient in the underwater environment can vary from 0.02 to 2.38 m^{-1}, and here we selected c = 0.15 m^{-1} and 0.305 m^{-1} in the investigation to compare the received signal optical power obtained using our theoretical model and two types of MC simulations. The results are shown in Fig. 4(c). It is clear that the received signal power reduces with the attenuation coefficient c, which is mainly due to the higher path loss. In addition, the MC results agree well with our theoretical results in sea water with different turbidity, which further verifies the accuracy of our theoretical model.

We also verified our solar background light model by MC simulations, where n solar photons were generated and they propagated in the same direction. The wavelength and optical power distribution of photons followed the solar spectrum irradiance provided in reference [32], as shown in Fig. 2. Whilst this data is for particular weather conditions and locations, we use it to investigate the impact of sun light incident angle. The solar photons first passed through the air-water interface following (8), and then propagated through the pure sea channel. If the solar photon interacted with the particle in water, the same process as that of the signal photon was followed. For the solar photons that reached the receiver, we recorded the power of each photon after passing through the TFF.

In the solar part, we investigated the received background light power and the corresponding CIR when changing the incident angle. Both theoretical and MC results are shown in Fig. 5. In the MC simulation, both the HG and TTHG scattering models were considered. It can be seen that the received solar power calculated by our theoretical model is slightly lower than MC results, due to the incorporation of scattering in MC simulations.

However, the difference is only around 0.2 dB. Similar with the signal light case, our proposed model can capture the dependence of received background light power on the incident angle. In addition, the CIR results are similar with those of the signal light, where the number of photons arriving after scattering is also much less than that arriving directly.

We also investigate the received background light power in sea water with different turbidity. Both theoretical and MC results are shown in Fig. 5(c). Similar to the signal part, it can be seen that due to the higher path loss, the received solar power decreases in sea water with a larger attenuation coefficient. More importantly, the results calculated using our proposed model agree well with the MC results under all conditions, showing the wide applicability of our proposed both signal and solar theoretical model.

C. Impact of Incident Angles on LOS UOWC System Performance

From the results shown in Section II-B, it can be seen that the incident angles of both signal and sun lights affect the UOWC system performance significantly. Hence, in this section, we further investigate the system SNR and BER under different incident angles. We first set $H_{LED} = 10$ m, $D_{TR} = 10$ m, and the bandwidth $B = 10$ MHz, as shown in Fig. 6(a). Using the proposed theoretical model, the LED orientation angle and the sun light radiation angle can be set in any value, and here we set them at 95.71° and -21.8° to investigate the impact of incident angles on the UOWC system. The two TFFs detailed in Section II-B were considered, and the SNR performance was studied [11], [13] when the PD was rotated, where the PD rotation angle $\alpha_{PD} = 0^\circ$ when the PD points at the LED directly, and α_{PD} is positive when the PD rotates in the clockwise direction.

The SNR results are shown in Fig. 6(b), where the results using previous theoretical models [11], [13] are also shown. Due to the assumption of constant transmittance at the receiver, the fluctuation of SNR with respect to the signal and solar light incident angles cannot be modeled using previous models. In addition, the previous models underestimate the SNR, which is caused by the overestimation of solar power when not considering the dependence of TFF transmittance on the solar light incident angle. Furthermore, as discussed in Section II-A, due to the different changes of signal power and solar power with respect to the incident angle (equivalently α_{PD}), the SNR performance is not optimal when the PD directly faces the LED. For the TFFs considered, the best SNR is achieved at non-zero PD rotation angle, where the SNR is 1.25 dB or 1.04 dB better depending on TFF considered, compared with the typical configuration where the PD directly faces the LED. Compared with TTF1, using TTF2 achieves better SNR. This is mainly because TFF2 has a broader passband as shown in Fig. 3, resulting in a higher received signal power.

The SNR performance under different PD depths is shown in Fig. 6(c). It is clear that SNR decreases with the increment of PD depth. This is mainly due to the rapid drop of the signal light power, which is caused by the large signal divergence. The impact of PD radius is further studied and the results are shown in Fig. 6(d). A better SNR is achieved with a larger PD radius, due to more signal power being collected and detected. However, when the PD radius exceeds 3 inches, the SNR improvement becomes smaller when further increasing it. This is due to the Lambertian signal light power distribution that decreases rapidly when moving away from the center.

In addition to SNR, the impact of incident angle on BER has also been studied, where the system configuration considered is shown in Fig. 6(e). We set the LED orientation angle and the sun light radiation angle at 135° and -70.05° so that the sun light propagates in the same direction as the signal light when the LED points at the PD directly, $H_{LED} = 10$ m and $B = 10$ MHz.

The BER performance is shown in Fig. 6(f). Similarly, due to not considering incident angles, previous models overestimate the BER. For the two TFFs considered in our proposed model TFF2 achieved better BER, consistent with the SNR result shown in Fig. 6(b). The impact of transmission distance on the BER performance is shown in Fig. 6(g). It can be seen that a better BER is achieved with a shorter transmission distance, due to the slower decrease of the signal power compared with the decrease of solar power when increasing the transmission distance. Finally, we also studied the BER with different PD radius, which is shown in Fig. 6(h). The BER is worse with a smaller PD radius, and similar with SNR, BER improvement also becomes smaller when further increasing the PD radius beyond 3 inches.

III. NLOS UOWC System and Simulation

A. NLOS Theoretical Model

Whilst the LOS communication link is widely used in UOWC systems to achieve high-speed wireless communication, in practical underwater environments marine lives and reefs can block the channel. To overcome this limitation, NLOS-based UOWC systems, which use the water-air surface to reflect the signal to avoid obstacles, are important in practice. Here, we consider a NLOS communication channel shown in Fig. 7, where the transmitter is steered to the ocean-air surface. Similar to the LOS model discussed above, the impact of light incident angles on the system performance needs to be considered for accurate modeling.

As shown in Fig. 7, we consider the flipped location of the receiver against the water surface as the virtual receiver, due to the use of specular reflection at the water-air surface in the NLOS system, the reflected signal needs to be considered, whilst the refracted signal at the interface forms part of the channel loss. Since the reflection angle is identical to the signal incident angle, the position of the virtual receiver and the position of the real receiver follow a mirror image relationship. The signal light emitted towards the virtual receiver can reach the physical receiver after the NLOS channel. We define the signal transit point as the intersection point between the ocean-air surface and the direction connecting the LED and the virtual receiver. Similar to the LOS case, the general turbidity in seawater also leads to signal path loss in the NLOS channel. Using (1), the

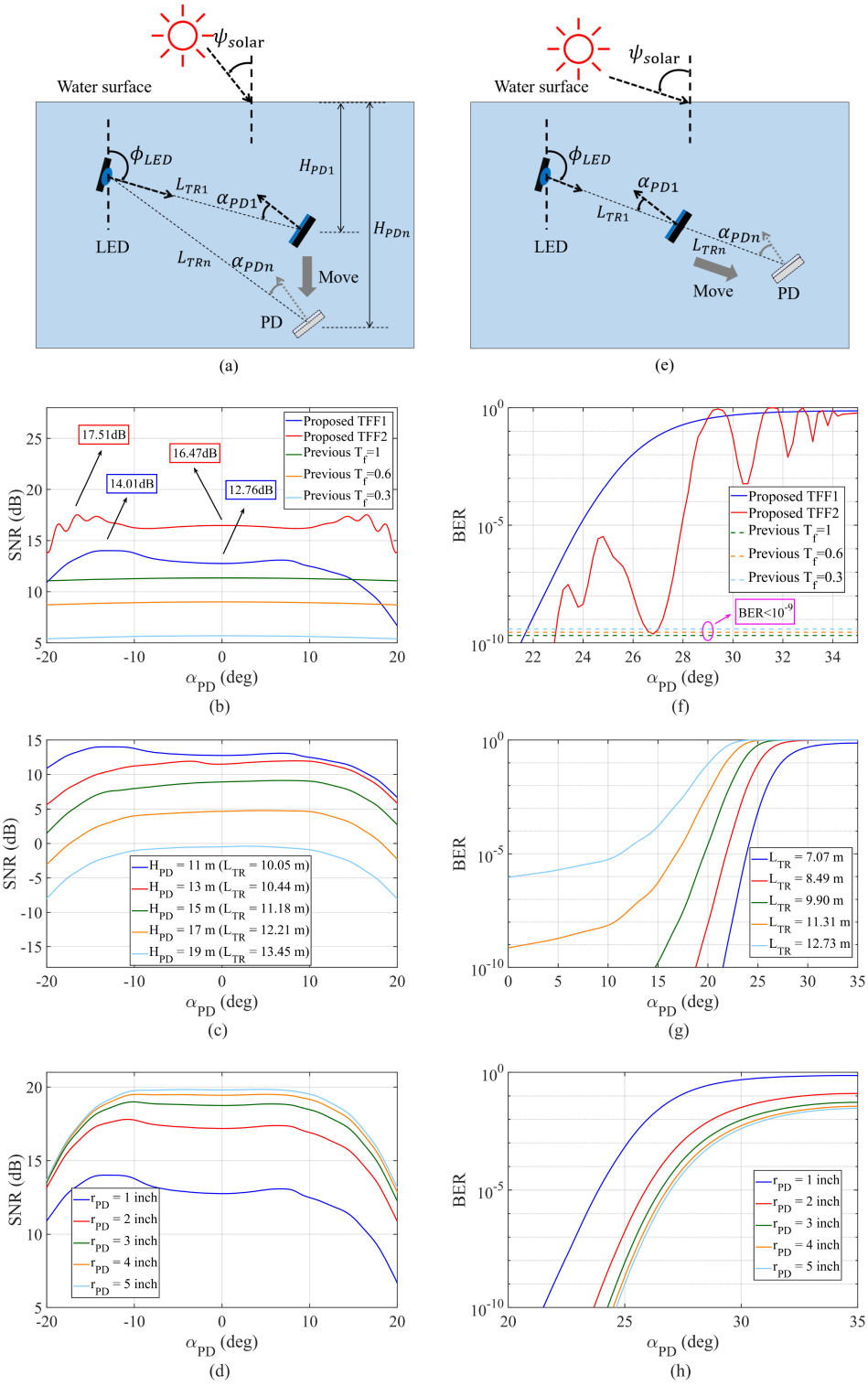

Fig. 6. LOS link results. (a): LOS configuration for SNR simulations; (b): SNR v.s. α_{PD} ($H_{PD} = 11$ m, and $r_{PD} = 1$ inch); (c): SNR v.s. α_{PD} with different PD depth (TFF1, and $r_{PD} = 1$ inch); (d): SNR v.s. α_{PD} with different PD radius (TFF1, and $H_{PD} = 11$ m); (e): LOS configuration for BER simulations; (f): BER v.s. α_{PD} ($D_{TR} = 5$ m, $H_{PD} = 15$ m, and $r_{PD} = 1$ inch); (g): BER v.s. α_{PD} with different distances (TFF1, and $r_{PD} = 1$ inch); (h): BER v.s. α_{PD} with different PD radius (TFF1, $D_{TR} = 5$ m, and $H_{PD} = 15$ m).

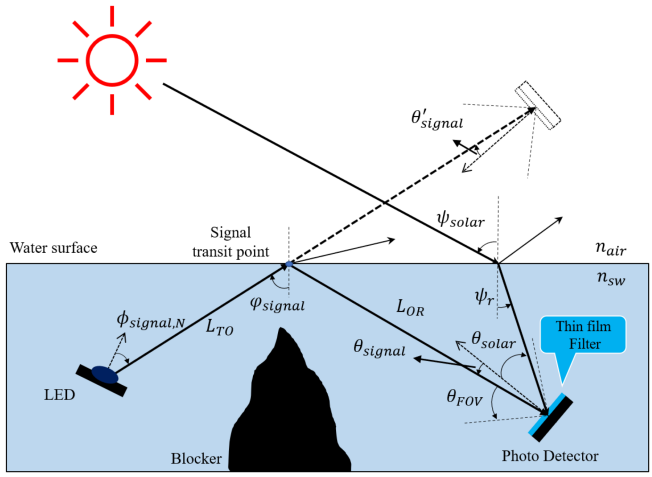

Fig. 7. NLOS UOWC system architecture.

NLOS signal path loss can be calculated as:

$$L_{signal,p,N}(\lambda) = e^{-c(\lambda)L_{TR,N}} = e^{-[a(\lambda)+b(\lambda)]L_{TR,N}}, \quad (16)$$

where $L_{TR,N} = L_{TO} + L_{OR}$ is the optical path length between the LED and the PD, and L_{TO} and L_{OR} are the Euclidean distance between the LED and the signal transit point and the distance between the signal transit point and the receiver, respectively.

When the signal light reaches the ocean-air surface, part of the light refracts to the air, and the remaining signal light reflects towards the receiver, introducing the signal reflection loss $L_{signal,r}$, which can be expressed as (17), shown at the bottom of the page, where $\varphi_c = \arcsin(\frac{n_{air}}{n_{sw}})$, and φ_r stands for the refraction angle of the signal at the ocean-air surface. Following the Snell's law, $\varphi_r = \arcsin(\frac{n_{sw}}{n_{air}}\sin(\varphi_{signal}))$. When $\varphi_{signal} \geq \varphi_c$, the signal light undergoes total reflection.

Similar to the LOS link, due to the beam divergence of the LED and the small aperture size of the receiver, there is also NLOS geometrical loss, which is expressed as

$$L_{signal,g,N} = \frac{m+1}{2\pi}\cos^m(\phi_{signal,N})\Delta\Omega_N, \quad (18)$$

where $\phi_{signal,N}$ denotes the LED radiation angle with respect to the virtual receiver as shown in Fig. 7, and $\Delta\Omega_N$ is the solid angle subtended by the virtual receiver differential area. Assuming $A_f << L^2_{TR,N}$, the solid angle is $\Delta\Omega_N = \frac{A_f \cos\theta_{signal}}{L^2_{TR,N}}$.

Finally, after passing through the TFF, the signal power reaching the PD can be expressed as (19), shown at the bottom of the page. Combining the signal electrical power with the noise variance, the SNR of the NLOS link is (20), shown at the bottom of the page. Similar with LOS system, when the OOK modulation format is used, the BER of NLOS UOWC system can be expressed as

$$BER_{NLOS,OOK} = \frac{1}{2}erfc\left(\frac{SNR_{NLOS}}{2\sqrt{2}}\right). \quad (21)$$

B. Monte-Carlo Verification of NLOS Channel Model

Similar to the LOS case, we also verified our NLOS channel model using MC simulations. The process is similar to that in the LOS case, with the exception of considering additional photon reflection at the ocean-air interface, where we recorded photon incident angles to determine if there was total internal reflection. There was no power loss under total internal reflection, and otherwise, a portion of power was lost following (17). After reflection, the same process was considered. If the photons reached the receiver, we recorded the power of each photon after passing through the optical filter. In the NLOS study, we set the LED and PD depth at $H_{LED} = 5$ m and $H_{PD} = 5$ m, and the horizontal distance between LED and PD D_{TR} at 10 m. The same $r_{PD} = 1$ inch and $n = 2 \times 10^8$ were considered. We also fixed θ_{PD} at $-45°$, $-25°$ or $-5°$, and changed the LED orientation angle ϕ_{LED} while investigating the system performance. We calculated theoretical received optical power using (19), and compared it with MC simulations adopting the HG and TTHG scattering models. The results are shown in Fig. 8(a).

Similar to the LOS link, due to scattering, the received signal power in MC simulations is slightly higher than the theoretical result, which verifies the accuracy of our NLOS UOWC model in the pure sea channel. Furthermore, due to the Lambertian pattern of the LED radiation, when the LED is rotated towards the transit point ($\phi_{LED} = 45°$ when LED directly faces the transit point), the signal strength increases. On the other hand, under the same LED orientation angle, the received signal power decreases when θ_{PD} changed from $-45°$ to $-5°$. This is mainly due to the smaller filter transmittance that reduces the collected signal power at larger incident angles. Comparing with Fig. 4(a), it is clear that due to a large part of light being refracted into the air as discussed in Section III-A, the NLOS link has a much lower received signal power than the LOS link. In addition, the

$$L_{signal,r} = \begin{cases} \frac{1}{2}\left[\left(\frac{\tan(\varphi_r-\varphi_{signal})}{\tan(\varphi_r+\varphi_{signal})}\right)^2 + \left(\frac{\sin(\varphi_r-\varphi_{signal})}{\sin(\varphi_r+\varphi_{signal})}\right)^2\right], & 0 < \varphi_{signal} \leq \varphi_c \\ 1, & \varphi_{signal} > \varphi_c \end{cases} \quad (17)$$

$$P_{signal,r,NLOS} = \begin{cases} \int_{\lambda_{LED,l}}^{\lambda_{LED,h}} P_t(\lambda)L_{signal,p,N}(\lambda)L_{signal,r}L_{signal,g,N}T_f(\lambda,\theta_{signal})d\lambda, & 0 \leq \theta_{signal} \leq \theta_{FOV} \\ 0. & \theta_{signal} > \theta_{FOV} \end{cases} \quad (19)$$

$$SNR_{NLOS} = \frac{\mu^2_{signal,NLOS}}{\sigma^2_{total,N}} = \frac{(\Re P_{signal,r,NLOS})^2}{2q\Re P_{solar.r}B + 2q\Re P_{blackbody}B + 2qI_{DC}B + 2q\Re P_{signal,r,NLOS}B + \frac{4kT_eFB}{R_L}} \quad (20)$$

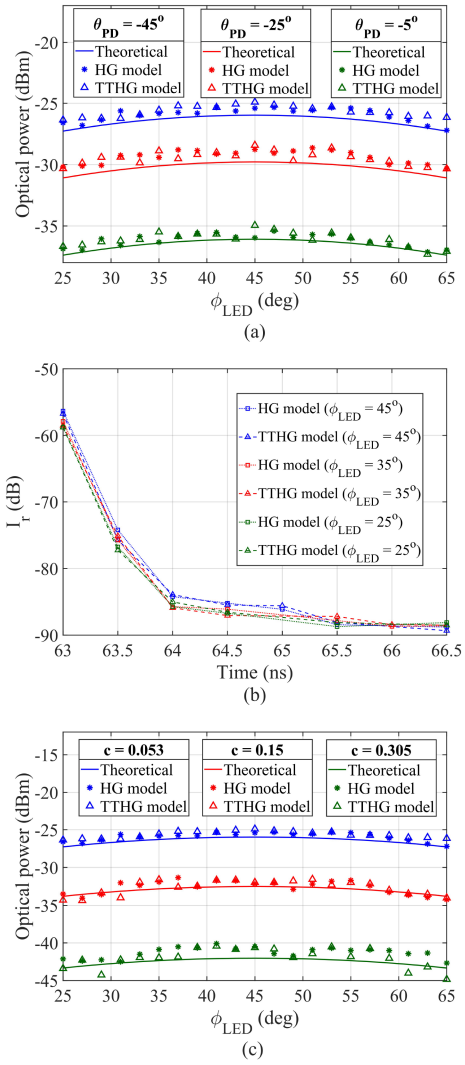

Fig. 8. NLOS theoretical and MC simulation results. (a): received signal optical power v.s. LED orientation angle ϕ_{LED}; (b): CIR under the PD orientation angle $\theta_{PD} = -45°$; (c): received signal optical power v.s. LED orientation angle ϕ_{LED} under different attenuation coefficient c ($\theta_{PD} = -45°$).

CIR under three LED orientation angles are also studied and the results are shown in Fig. 8(b). It is clear that due to the small number of photons arriving at the receiver after scattering, the optical power drops sharply with time. Hence, the impact of scattering is also negligible in the pure sea water NLOS channel considered here.

Furthermore, we also investigate the received signal power under different attenuation coefficients c in the NLOS link. The results are shown in Fig. 8(c). Similar with the LOS link case shown in Fig. 4(c), the theoretical results also agree well with simulations in the NLOS link under all water conditions. Due to a longer path length and the additional signal reflection at the water-air interface, the NLOS link has a much lower received signal power than the LOS link.

It worth mentioning that if the blocker shown in Fig. 7 reaches the height of water-air interface, it will result in the received signal power $P_{signal,r,NLOS} = 0$, due to the complete blocking of communication channel. In this situation, the use of relay can be explored. For example, underwater relay nodes can be used to bypass such extreme blockers [13]. With underwater relay nodes, the effective channel is always below the water surface and the channel direction can be changed multiple times to establish an UOWC link avoiding such blockers. However, this method requires relay nodes being deployed underwater, the simple amplify and forward type of relay node may lead to degraded data transmission quality, and efficient networking algorithms need to be developed. In addition to underwater relay nodes, above water relay nodes such as UAVs (Unmanned Aerial Vehicle) can also be explored [33]. In this case, the optical signal propagates through the water-air surface twice and extra UAVs are needed, leading to additional losses and higher cost. Whilst recent studies show the feasibility of relay assisted UOWCs, more detailed studies are required in the future.

C. Impact of Incident Angles on NLOS UOWC System Performance

Similar to the LOS system, we further investigate the impact of light incident angles on the NLOS system SNR and BER. We first set the LED orientation angle and the sun light radiation angle at $45°$ and $16.7°$, $H_{LED} = 5$ m, and $D_{TR} = 10$ m, as shown in Fig. 9(a). The same TFFs were used here. It is noted that due to the high reflection loss in NLOS links, NLOS links are mainly used to maintain wireless connectivity at a lower speed when LOS links are blocked. Hence, here we adjusted the bandwidth to $B = 100$ kHz accordingly. In the NLOS system, we define $\alpha_{PD,N} = 0$ when the PD points at the transit point, and $\alpha_{PD,N}$ is positive when the PD rotates in the clockwise direction.

The SNR results under different TFFs are shown in Fig. 9(b), where results obtained using previous models [13] are also shown. Similar to the LOS system, due to not considering incident angles, the previous model underestimate the SNR. Moreover, using TFF2 achieves much better SNR compared with TFF1. Compared with the LOS case, the SNR improvement using TFF2 instead of TFF1 in the NLOS system is larger. This is mainly due to the high reflection loss at the water surface, where any increase of signal power has a large influence on SNR. More importantly, due to different changes of signal and sun lights powers with respect to the incident angle, the best SNR is also achieved at non-zero PD rotation angle, where an improvement of 0.69 dB and 1.05 dB is achieved using TFF1 and TFF2, respectively. The impact of PD depths and PD radius on the SNR performance are also studied, with the results shown in Fig. 9(c) and (d), respectively. It is clear that because the signal light power drops rapidly when the receiver depth increases, the SNR decreases as well. Furthermore, a better SNR is achieved with larger PD radius.

We further studied the impact of incident angle on BER in the NLOS system, where the system configuration considered is shown in Fig 9(e). We set the LED orientation angle and the sun light direction angle at $45°$ and $-70.05°$ so that the sun light propagates in the same direction as the reflected signal light, $H_{LED} = 5$ m and $B = 10$ kHz. The BER performance is shown

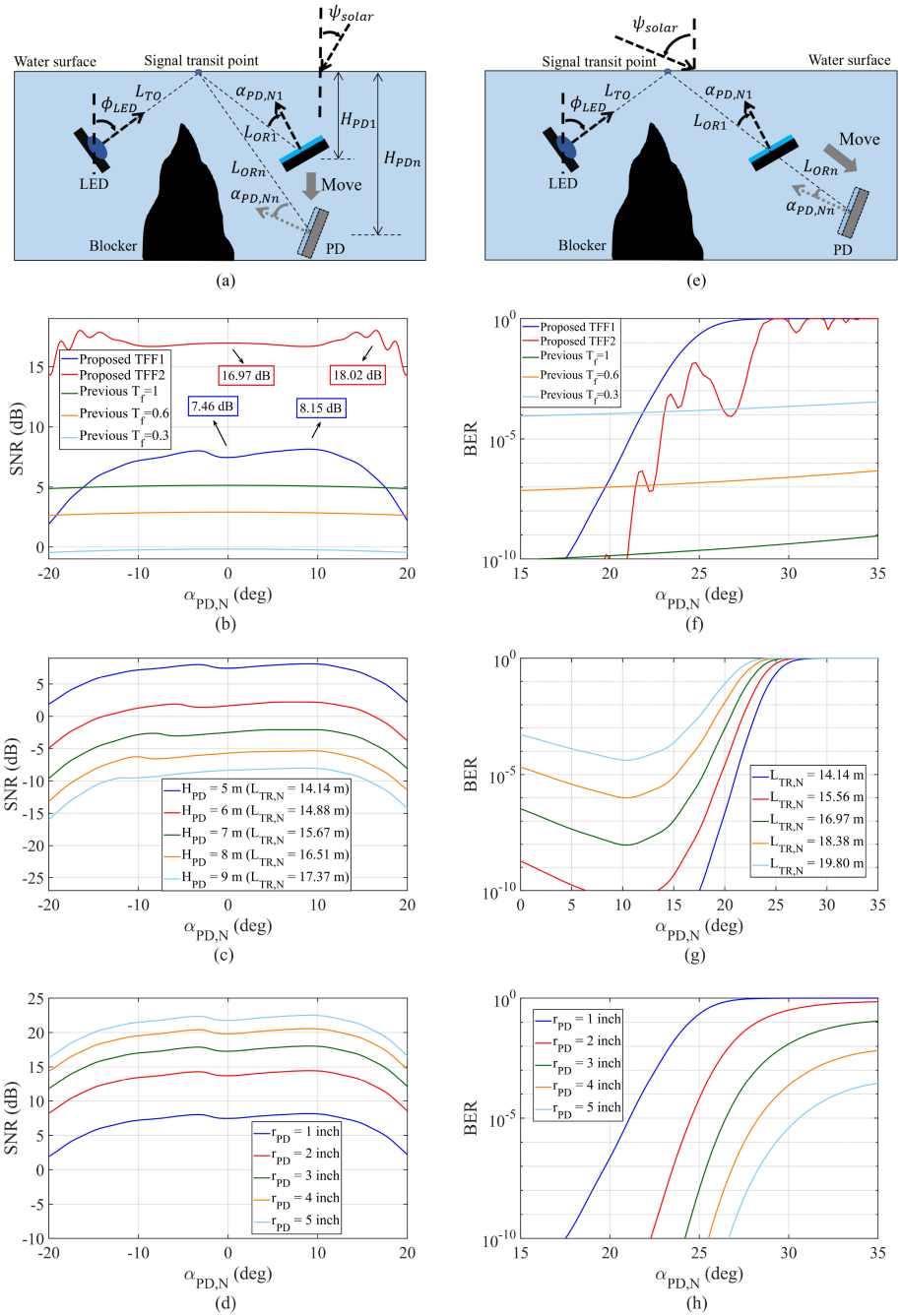

Fig. 9. NLOS link results. (a): NLOS configuration for SNR simulations; (b): SNR v.s. $\alpha_{PD,N}$ ($H_{PD} = 5$ m, and $r_{PD} = 1$ inch); (c): SNR v.s. $\alpha_{PD,N}$ with different PD depth (TFF1, and $r_{PD} = 1$ inch); (d): SNR v.s. $\alpha_{PD,N}$ with different PD radius (TFF1, and $H_{PD} = 5$ m); (e): NLOS configuration for BER simulations; (f): BER v.s. $\alpha_{PD,N}$ ($D_{TR} = 10$ m, $H_{PD} = 5$ m, and $r_{PD} = 1$ inch); (g): BER v.s. $\alpha_{PD,N}$ with different distances (TFF1, and $r_{PD} = 1$ inch); (h): BER v.s. $\alpha_{PD,N}$ with different PD radius (TFF1, $D_{TR} = 10$ m, and $H_{PD} = 5$ m).

in Fig 9(f), where it is clear that the previous models underestimate the BER at small PD rotation angles and overestimate it at large angles. Similar with the LOS case, TFF2 achieved better BER. The impact of PD depths are shown in Fig. 9(g). Under the same transmission distance, when $\alpha_{PD,N}$ increases, the BER first becomes better, which is due to the faster decrease of sun light power than the signal light. However, when $\alpha_{PD,N}$ is large, the change of filter transmittance becomes more dominant, leading to a worse BER when further increasing $\alpha_{PD,N}$. Similar to the LOS case, the BER is better with a shorter transmission distance. The impact of PD radius on BER are further shown in Fig. 9(h). Due to the same reason as the LOS system discussed above, the BER is worse with a smaller PD radius.

IV. Conclusion

In this paper, we have established an accurate UOWC mathematical model with both LOS and NLOS links, where the overlooked impact of light incident angles in previous studies

has been incorporated. The proposed UOWC model has been verified by MC simulations. Results have shown that the discrepancy is minimal and our proposed theoretical results agree well with MC simulations, which verifies the accuracy of both LOS and NLOS UOWC model in pure sea channel. In addition, we have also studied the impact of incident angles on the SNR and the BER performance using the proposed model. Results have shown that the incident angles of both signal and sun lights have significant impact on the system performance in both LOS and NLOS channels, which cannot be captured accurately using previous models. Furthermore, we have applied the proposed model to optimize the receiver orientation to maximize the achievable SNR in UOWC systems. Results have shown that compared with the transmitter and the receiver directly pointing at each other, optimizing the receiver orientation angle can further improve the SNR performance due to the better rejection of background light. Therefore, our proposed model provides a more accurate theoretical framework for UOWC studies and system designs.

REFERENCES

[1] E. Sozer, M. Stojanovic, and J. Proakis, "Underwater acoustic networks," *IEEE J. Ocean. Eng.*, vol. 25, no. 1, pp. 72–83, Jan. 2000.

[2] M. Stojanovic, "Recent advances in high-speed underwater acoustic communications," *IEEE J. Ocean. Eng.*, vol. 21, no. 2, pp. 125–136, Apr. 1996.

[3] I. Akyildiz, D. Pompili, and T. Melodia, "Challenges for efficient communication in underwater acoustic sensor networks," *SIGBED Rev.*, vol. 1, no. 2, pp. 3–8, 2004.

[4] A. Al-Shamma'a, A. Shaw, and S. Saman, "Propagation of electromagnetic waves at MHz frequencies through seawater," *IEEE Trans. Antennas Propag.*, vol. 52, no. 11, pp. 2843–2849, Nov. 2004.

[5] P. Tian, A. Sturniolo, A. Messa, D. Scaradozzi, and E. Ciaramella, "High-speed underwater optical wireless communication using a blue GaN-based micro-LED," *Opt. Exp.*, vol. 25, no. 2, pp. 1193–1201, 2017.

[6] C.-Y. Li et al., "A 5 m/25 gbps underwater wireless optical communication system," *IEEE Photon. J.*, vol. 10, no. 3, pp. 1–9, Jun. 2018, Art. no. 7904909.

[7] S. Zhu, X. Chen, X. Liu, G. Zhang, and P. Tian, "Recent progress in and perspectives of underwater wireless optical communication," *Prog. Quantum Electron.*, vol. 73, 2020, Art. no. 100274.

[8] H. Chen et al., "Toward long-distance underwater wireless optical communication based on a high-sensitivity single photon avalanche diode," *IEEE Photon. J.*, vol. 12, no. 3, pp. 1–10, Jun. 2020, Art. no. 7902510.

[9] J. Giles and I. Bankman, "Underwater optical communications systems. part 2: Basic design considerations," in *Proc. MILCOM IEEE Mil. Commun. Conf.*, 2005, vol. 3, pp. 1700–1705.

[10] S. Jaruwatanadilok, "Underwater wireless optical communication channel modeling and performance evaluation using vector radiative transfer theory," *IEEE J. Sel. areas Commun.*, vol. 26, no. 9, pp. 1620–1627, Dec. 2008.

[11] T. Hamza, M.-A. Khalighi, S. Bourennane, P. Léon, and J. Opderbecke, "Investigation of solar noise impact on the performance of underwater wireless optical communication links," *Opt. Exp.*, vol. 24, no. 22, pp. 25832–25845, 2016.

[12] X. Wang, M. Zhang, H. Zhou, and X. Ren, "Performance analysis and design considerations of the shallow underwater optical wireless communication system with solar noises utilizing a photon tracing-based simulation platform," *Electron. (Basel)*, vol. 10, no. 5, 2021, Art. no. 632.

[13] F. Xing and H. Yin, "Performance analysis for underwater cooperative optical wireless communications in the presence of solar radiation noise," in *Proc. IEEE Int. Conf. Signal Process., Commun. Comput.*, 2019, pp. 1–6.

[14] F. Xing, H. Yin, X. Ji, and V. C. M. Leung, "Joint relay selection and power allocation for underwater cooperative optical wireless networks," *IEEE Trans. Wireless Commun.*, vol. 19, no. 1, pp. 251–264, Jan. 2020.

[15] R. Boluda-Ruiz, P. Rico-Pinazo, B. Castillo-Vázquez, A. García-Zambrana, and K. Qaraqe, "Impulse response modeling of underwater optical scattering channels for wireless communication," *IEEE Photon. J.*, vol. 12, no. 4, pp. 1–14, Aug. 2020, Art. no. 7904414.

[16] C. Gabriel, M.-A. Khalighi, S. Bourennane, P. Léon, and V. Rigaud, "Monte-Carlo-based channel characterization for underwater optical communication systems," *J. Opt. Commun. Netw.*, vol. 5, no. 1, pp. 1–12, 2013.

[17] V. I. Haltrin, "Chlorophyll-based model of seawater optical properties," *Appl. Opt. (2004)*, vol. 38, no. 33, pp. 6826–6832, 1999.

[18] J. R. a. Barry, *Wireless Infrared Communications*. Springer, 1994.

[19] H. A. Macleod, *Thin-Film Optical Filters.*, 5th ed., (Series in Optics and Optoelectronics Series). Milton, U.K.: Taylor and Francis Group, 2017.

[20] D. M. Topasna and G. A. Topasna, "Numerical modeling of thin film optical filters," in *Education and Training in Optics and Photonics*. Optica Publishing Group, 2009, pp. 96661P–96661P–10.

[21] X. Wang, M. Zhang, H. Zhou, and X. Ren, "Performance analysis and design considerations of the shallow underwater optical wireless communication system with solar noises utilizing a photon tracing-based simulation platform," *Electronics*, vol. 10, no. 5, 2021, Art. no. 632.

[22] M. Sui, X. Yu, and F. Zhang, "The evaluation of modulation techniques for underwater wireless optical communications," in *Proc. Int. Conf. Commun. Softw. Netw.*, 2009, pp. 138–142.

[23] M. A. A. Ali and A. Ali, "Characteristics of optical channel for underwater optical wireless communication based on visible light," *Australian J. Basic Appl. Sci.*, vol. 9, no. 23, pp. 437–445, 2015.

[24] LUMILEDS, "Lxml-pr02-a900 rebel led datasheet," 2017. [Online]. Available: https://www.luxeonstar.com/assets/downloads/ds68.pdf

[25] L. Tao, Z. Hongming, and S. Jian, "Distribution of arriving angle of signal in underwater scattering channel," *Chin. J. Lasers*, vol. 45, no. 11, 3 2018, Art. no. 306003. [Online]. Available: https://www.researching.cn/articles/OJe640e3ff3b289f24

[26] F. Llya, "Blue led thin film narrow band-pass filter," 2016. [Online]. Available: https://www.slideshare.net/IlyaFedarovich/blue-led-thin-film-narrow-bandpass-filter-design-project

[27] Avago Technologies, "Hlmp-cb3a-uv0dd rebel led datasheet," 2013. [Online]. Available: https://www.farnell.com/datasheets/1918236.pdf

[28] G. J. Blinowski, "The feasibility of launching rogue transmitter attacks in indoor visible light communication networks," *Wireless Pers. Commun.*, vol. 97, no. 4, pp. 5325–5343, 2017.

[29] H. Nguyen et al., "A MATLAB-based simulation program for indoor visible light communication system," in *Proc. 7th Int. Symp. Commun. Syst., Netw. Digit. Signal Process.*, 2010, pp. 537–541.

[30] R. Gonçalves-Araujo and S. Markager, "Light in the dark: Retrieving underwater irradiance in shallow eutrophic waters from AC-S measurements," *Front. Mar. Sci.*, vol. 7, 2020, Art. no. 343.

[31] B. Nababan, D. Ulfah, and J. Panjaitan, "Light propagation, coefficient attenuation, and the depth of one optical depth in different water types," in *Proc. IOP Conf. Ser.: Earth Environ. Sci.*, vol. 944, no. 1, 2021, Art. no. 0 12047.

[32] National Centers for Environmental Information, "Spectral solar irradiance," 2017. [Online]. Available: https://www.ncei.noaa.gov/thredds/catalog/cdr-spectral-solar-irradiance/daily/catalog.html

[33] T. Lin, C. Gong, J. Luo, and Z. Xu, "Dynamic optical wireless communication channel characterization through air-water interface," in *Proc. IEEE/CIC Int. Conf. Commun. China (Workshops)*, 2020, pp. 173–178.